Effect of Surface Roughness of Carbon Nanotube-based Catalyst Layer for Polymer Electrolyte Membrane Fuel Cell Performance

Journal:	*Sustainable Energy & Fuels*
Manuscript ID	SE-ART-06-2022-000857.R2
Article Type:	Paper
Date Submitted by the Author:	02-Sep-2022
Complete List of Authors:	Phua, Yin Kan; Kyushu University Faculty of Engineering Graduate School of Engineering Weerathunga, Don Terrence; Kyushu University Faculty of Engineering Graduate School of Engineering Wu, Dan; Kyushu University Kim, Chaerin; Kyushu University International Institute for Carbon-neutral Energy Research Jayawickrama, Samindi; Kyushu University Faculty of Engineering Graduate School of Engineering; Kyushu University International Institute for Carbon-neutral Energy Research Tanaka, Naoki; Kyushu University, Applied Chemistry Fujigaya, Tsuyohiko; Kyushu Daigaku Kogakubu Daigakuin Kogakufu,

SCHOLARONE™
Manuscripts

Effect of Carbon Nanotube-based Catalyst Layer Surface Roughness on Polymer Electrolyte Membrane Fuel Cell Performance

Yin Kan Phua [a], *Don Terrence Dhammika Weerathunga* [a, b]*, Dan Wu* [a]*, Chaerin Kim* [b]*,*

Samindi Madhubha Jayawickrama [a, b]*, Naoki Tanaka* [a, b]*, Tsuyohiko Fujigaya* [a, b, c, *]

[a] Department of Applied Chemistry, Graduate School of Engineering, Kyushu University,

744 Motooka, Nishi-ku, Fukuoka 819-0395, Japan

[b] International Institute for Carbon Neutral Energy Research, Kyushu University, 744

Motooka, Nishi-ku, Fukuoka 819-0395, Japan

[c] Center for Molecular Systems, Kyushu University, 744 Motooka, Nishi-ku, Fukuoka

819-0395, Japan

Corresponding author

E mail address: fujigaya.tsuyohiko.948@m.kyushu-u.ac.jp (T. Fujigaya)

Telephone/Fax: +81-92-802-2842

1

Abstract

Polymer Electrolyte Membrane Fuel Cells (PEMFCs) play a centralized role in the

decarbonization of energy system due to its carbon-free electricity generation. However, low

utilization efficiency of its Pt electrocatalyst has hindered PEMFCs from widespread adoption.

Herein, the effect of surface roughness on a catalyst layer (CL) based on carbon nanotubes (CNTs)

in contact with polymer electrolyte membranes (PEMs) in PEMFCs was studied to examine the

relationship between such surface roughness and Pt utilization efficiency. The surface roughness

of the vacuum-filtered CL sheets was evaluated using a laser microscope. The surface of the CL

sheet contacting the filter membrane was smoother than that of the surface exposed to air. When

the CL sheet with the smoother surface was laminated with the PEM to fabricate a membrane

electrode assembly (MEA), the power density of the single cell was 604.6 mW cm^{-2} at 80 °C

under 100% relative humidity (RH), which was greater than that of the MEA with a rougher CL

surface (542.4 mW cm^{-2}).

1. Introduction

The global demand for clean and sustainable energy has driven the development of fuel cells,

which allow the use of hydrogen as an energy source and generate electricity without emitting

carbon dioxide during energy conversion [1-5]. Owing to their low operating temperature, device

compactness, and silent operation, polymer electrolyte membrane fuel cells (PEMFCs) have been

intensively researched for applications ranging from portable devices to stationary power supplies

[4-6]. Despite the advantages of PEMFCs, major improvements must be made before widespread

adoption can be realized, such as enhanced durability and initial power generation efficiency [6].

Platinum (Pt) electrocatalysts play a key role in determining PEMFC durability, as a decrease in the Pt surface area is a major cause of PEMFC deterioration. Numerous studies have been conducted to improve PEMFC durability [7-10]. It is known that the durability of the Pt carbon supports is a very important factor in improving the durability of Pt electrocatalysts, because carbon corrosion induces Pt agglomeration and decreases the Pt surface area [11, 12].

Carbon nanotubes (CNTs) have recently emerged as highly durable carbon supports that provide excellent durability for Pt electrocatalysts, as compared to conventional carbon supports such as carbon black (CB) [13-17]. This is due to the characteristic graphitized structure of CNTs, which is based on sp^2 carbons [18-20]. However, the lack of sp^3 carbons in CNTs makes homogeneous Pt deposition onto CNTs rather difficult, because sp^3 carbons act as anchoring sites for Pt [21, 22]. The chemical oxidation of CNTs has been applied to introduce anchoring sites and increase the number of sp^3 carbons [22-29], but doing so reduces durability [29, 30].

Previously, we demonstrated that the polymer coating of CNTs circumvents the need to introduce sp^3 carbons into the CNTs, while simultaneously providing anchoring sites for Pt. This allowed us to demonstrate the remarkable durability of PEMFCs based on these polymer-coated CNT electrocatalysts, as compared to conventional PEMFCs with CB-based electrocatalysts [31-35]. The remaining issue with CNT-based electrocatalysts is their lower initial power generation efficiency compared to that of CB-based electrocatalysts [36]. Owing to the unique one-dimensional fibrous structure of CNTs and their strong hydrophobicity, a catalyst layer (CL) composed of CNT-based electrocatalysts (CNT-CLs) possesses specific advantages in processability and structural controllability. This results in additional factors to consider when designing methods to improve the performance of CNT-CLs compared to those for improving the performance of CLs containing CB-based electrocatalysts (CB-CLs). One such additional consideration is the inferior mass diffusion of CNT-CLs compared to that of CB-CLs, which is caused by the fibrous morphology in the microstructure of the CNT-CLs [37]. To solve this problem, we incorporated polytetrafluoroethylene (PTFE) particles into CNT-CLs [38] to prevent water accumulation and

improve gas diffusion in the CNT-CLs [39, 40]. After incorporating PTFE particles into the CNT-CLs, the Pt utilization efficiency improved, but the maximum power density was still lower than that of PEMFCs based on CB-CLs.

To further improve mass diffusion in the CNT-CLs, we focused on the effect of the roughness of the CNT-CL surface that contacts the polymer electrolyte membrane (PEM). It has been pointed out that the fabrication method used for CLs strongly affects the degree of interfacial resistance between the PEM and CL. Research has been conducted on eliminating such resistance to improve the power density of PEMFCs based on CB-CLs [41-44]. However, there are no reports regarding the interfacial resistance between CNT-CLs and PEMs. In the preparation of CNT-CLs, agglomeration of the electrocatalyst slurry is always problematic, especially at high concentrations, owing to the hydrophobic and fibrous structure of CNTs; hence, CNT dispersions with low solid content (< 1.4 wt%) are often used to minimize agglomeration [45]. This is in contrast to the preparation of a CB-based electrocatalyst slurry with a high solid content (> 10 wt%) [46, 47]. Owing to the necessity of using a dilute CNT-based electrocatalyst slurry, the conventional decal transfer [48, 49] or blade coating [47, 50] techniques used for CB-CL preparation are difficult to apply to CNT-CLs. Similarly, spray coating [51, 52] is also unfavourable because it requires a high-concentration electrocatalyst slurry, which encourages CNT aggregation and risks clogging the spray nozzle.

Instead, the vacuum-filtration method, in which the catalyst slurry is filtered through either a gas diffusion layer (GDL) or a filter membrane [38, 53] to form a catalyst-coated GDL (**Scheme 1a**) or free-standing CL (**Scheme 1b**), respectively, is often used because it allows the use of a dilute dispersion [53, 54]. This method is also preferable for the practical fabrication of CNT-CLs because the process is simple, fast, and scalable [53, 54]. However, the effects of the degree of CNT-CL homogeneity on the CL surface roughness have not been investigated.
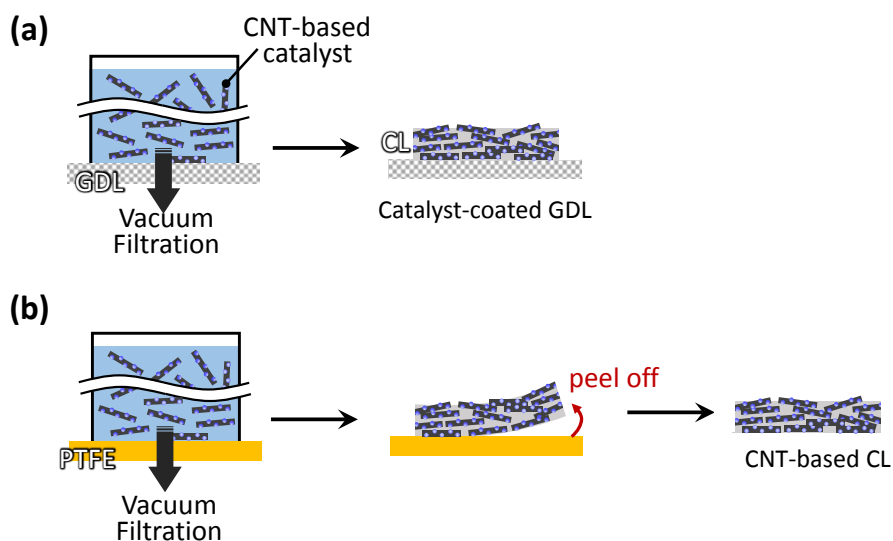
Scheme 1. Schematic of vacuum-filtration preparation of (a) catalyst-coated GDL and (b) free-standing CNT-based CL.

In this study, we investigated the effects of the surface roughness of CNT-CLs fabricated by the vacuum-filtration method on PEMFC performance. CNT-CLs with different surface roughnesses were laminated onto the PEM, and the cell performance was measured.

2. Experimental Procedures

2.1 Materials

Hydrogen hexachloroplatinate hexahydrate ($H_2PtCl_6 \cdot 6H_2O$), 2-propanol, *N, N*-dimethylacetamide (DMAc), and ethylene glycol (EG) were purchased from FUJIFILM Wako Pure Chemical Corporation (Tokyo, Japan). Nafion solution (5 wt%) in lower aliphatic alcohol and Nafion® 212 membranes were purchased from Sigma-Aldrich (MA, USA). Polybenzimidazole (PBI) (containing 23.4 wt% DMAc) was purchased from Sato Light Industrial Co., Ltd (Kameyama, Japan). Milli-Q ultra-pure water with a resistance of 15 MΩ cm was used in this study. The gas diffusion layer (Sigracet GDL-29BC) was purchased from the Fuel Cell Store (Texas, USA). Commercial gas diffusion electrodes (GDEs), EC-10-05-7, were purchased from Electrochem, Inc. (MA, USA). Multi-walled carbon nanotubes (CNTs) produced by

chemical vapor deposition (CVD) without the use of metal catalysts were generously provided by Nikkiso Co. (Tokyo, Japan).

2.2 Material characterization

Thermogravimetric analysis (TGA) was conducted using an EXSTAR TG/DTA7300 analyser (Hitachi High-Tech, Tokyo, Japan) at a heating rate of 10 °C min^{-1} under an air flow of 300 mL min^{-1} to determine the Pt loading of the formed CL. For Nafion content determination, a heating rate of 5 °C min^{-1} under a N_2 flow of 300 mL min^{-1} was first used for the temperature range 30 °C to 550 °C, followed by cooling to 200 °C under a N_2 atmosphere. The sample was then heated to 900 °C at an air flow rate of 300 mL min^{-1} and a heating rate of 10 °C min^{-1} [55]. Transmission electron microscopy (TEM) was performed using a JEM-2010 microscope (JEOL, Tokyo, Japan) operated at 120 kV. X-ray photoelectron spectroscopy (XPS) was performed using an AXIS-ULTRA DLD spectrometer (Shimadzu, Kyoto, Japan). Laser and optical microscope images were obtained using an industrial microscope OLS4000 (Olympus, Tokyo, Japan).

2.3 Fabrication of electrocatalysts

The electrocatalysts were fabricated using a method modified from our previous report [38]. CNTs (30 mg) were mixed with PBI (13 mg) in DMAc (40 mL) using a shear mixer L5M-A (Silverson, Buckinghamshire, United Kingdom). The obtained PBI-wrapped CNT (CNT/PBI) in DMAc solution was first centrifuged (33,600 *g*) and decanted, followed by the addition of a 20% 2-propanol solution (10 mL). This step was repeated three times to remove the unreacted PBI and remaining DMAc from the CNT/PBI solution. The decanted CNT/PBI in 2-propanol solution was then dispersed in 40 mL of a 60% (v/v) ethylene glycol (EG) solution by vigorous shaking. A calculated amount of 6.25 wt% $H_2PtCl_6 \cdot 6H_2O$ aqueous solution (1.062 g) dispersed in 60% (v/v) EG (60 mL) to obtain a Pt loading of 40 wt% was added to the CNT/PBI solution. The solution was then refluxed at 140 °C for 6 h under a N_2 atmosphere. The resulting composite (CNT/PBI/Pt)

solution was centrifuged (33,600 g) and decanted, followed by the addition of 5 mL of Milli-Q water. This step was repeated three times to remove the unreacted Pt precursor and remaining EG solution. The obtained decanted CNT/PBI/Pt solution was dispersed by vigorously shaking in 100 mL of 80% 2-propanol solution, sonicated for 10 min, and vacuum filtered through a PTFE filter membrane to obtain CNT/PBI/Pt sheets with a Pt loading of 0.35 mg cm^{-2}.

2.4 Fabrication of membrane-electrode-assemblies (MEAs)

To introduce the ionomer into the obtained electrocatalysts, the CNT/PBI/Pt sheets were cut into 1 cm × 1 cm pieces and dipped in a 1 wt.% Nafion solution (5 mL) [38] for 24 h at 25 °C, then dried under vacuum at room temperature for 2 h. The obtained CLs were hot-pressed with GDLs at 132 °C under 0.6 MPa for 20 s to fabricate the gas diffusion electrodes (GDEs). The Nafion membranes were sandwiched between the obtained GDEs (cathode) and commercial GDEs (anode), and hot pressed at 132 °C under 0.6 MPa for 20 s to obtain the MEAs (**Scheme 2**). CLs having I/C = 0.29 were prepared by dipping in a 0.5 wt.% Nafion solution (5 mL) in similar fashion.

2.5 Single cell measurements

The fabricated MEAs were assembled by using gaskets, bipolar plates, and current collectors. Fuel cell performance was evaluated according to the protocol provided by the New Energy and Industrial Technology Development Organization (NEDO) [56] using an in-house single-cell system (Auto PEM-ER01, TOYO Corporation, Tokyo, Japan). First, the MEA was activated for 20 h by applying a constant voltage (0.5 V) under 100% humidified H$_2$ (anode) and air (cathode) flowing at 0.139 L min^{-1} and 0.332 L min^{-1}, respectively, at 75 °C. Then, a galvanostatic condition was applied to obtain current–voltage polarization curves with a scan rate of 20 mA s^{-1}, scanning from low current to high current, using a SP-240 potentiostat (Bio-Logic Science Instruments, Seyssinet-Pariset, France), under the condition of 100% humidified H$_2$ (anode) and air (cathode)

flowing at 0.1 L min^{-1} and 0.2 L min^{-1}, respectively, at 80 °C. More than 30 scans were recorded to assure stable performance, and the representative polarization curves were displayed. Impedance spectra were obtained (frequency range 0.1 to 10 kHz) with a sinusoidal amplitude of 10% of the applied current. The equivalent circuit for impedance characterization is illustrated in **Figure S1**. Before in situ cyclic voltammetry (CV) was performed, activation by applying 100 potential cycles from 0.05 to 0.9 V vs. RHE with a 50 mV s^{-1} scan rate was done under a supply of 100% humidified H_2 (anode) and N_2 (cathode) flowing at 0.1 L min^{-1} and 0.2 L min^{-1}, respectively, at 40 °C.

Then, only the cathode N_2 gas supply was stopped, and in situ CV was performed by applying three potential cycles from 0.05 to 0.9 V vs. RHE with a 50 mV s^{-1} scan rate. The hydrogen desorption peak of the third CV cycle performed after the activation cycle was used to determine the electrochemically active surface area (ECSA) of the MEAs. All above measurements were done at atmospheric pressure, and no backpressure was applied.

3. Results and Discussion

3.1 Preparation of the catalyst composites and fabrication of the catalyst layers

Prior to Pt deposition, CNTs were coated with a polymer to introduce anchoring sites for the CNT surface [33]. Polybenzimidazole (PBI) was chosen as a coating polymer because of its excellent ability to anchor metal nanoparticles and coating homogeneity on carbon materials [57]. From the TEM image of the obtained composite (CNT/PBI/Pt) (**Figure 1a**), it is clear that Pt nanoparticles with a diameter distribution of 3.7 ± 1.3 nm were homogeneously dispersed on the CNT surface. In the XPS survey scan, the nitrogen N 1s peak was observed at approximately 400 eV [33], and Pt 4f doublet peaks for 4f$_{7/2}$ and 4f$_{5/2}$ were observed at 71.7 eV and 74.9 eV, respectively, suggesting that PBI was coated on the CNTs forming PBI-coated CNTs (CNT/PBI), and Pt was deposited onto CNT/PBI forming CNT/PBI/Pt (**Figure 1b**; for narrow scans, see **Figure S2a** and **S2b**). The

Pt loading percentage was determined to be 37 wt% using thermogravimetric analysis (TGA) based on the residual amount of the composite at 900 °C (**Figure 1c**). **Figure 1d** shows a photograph of the free-standing CNT/PBI/Pt sheet with a Pt content of 0.35 ± 0.025 mg cm^{-2}, fabricated through vacuum filtration of the CNT/PBI/Pt dispersion using PTFE as the filter membrane. It is worth noting that harsh treatments, such as probe sonication in the preparation step [38], resulted in films that could not be separated from the membrane (**Figure S3**), presumably due to shortening of the CNTs [58-60] that reduces the mechanical strength of the CNT sheets [60, 61].
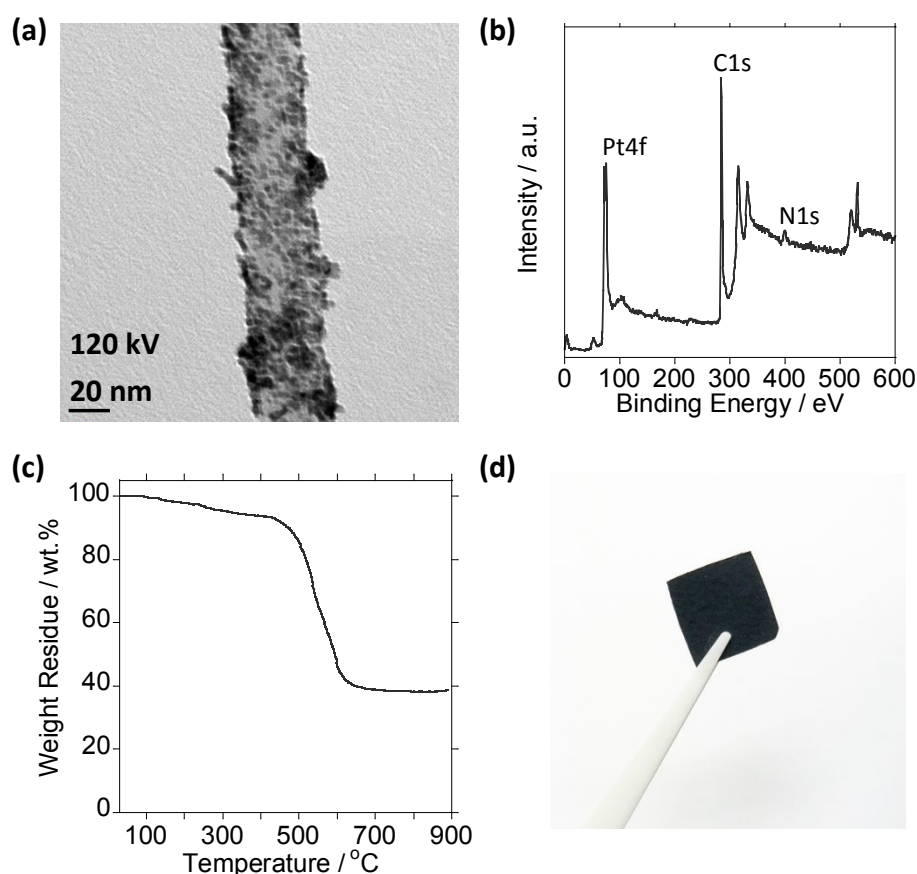

Figure 1. (a) TEM image measured at 120 kV, (b) XPS survey scan, and (c) TGA curve of the CNT/PBI/Pt. (d) Photograph of the free-standing CNT/PBI/Pt sheet.

Optical microscopy images of the sheet surfaces are shown in **Figure 2**. The images show that the bottom surface, which is directly in contact with the PTFE membrane during vacuum filtration, is smoother (**Figure 2a**) than that of the top surface, which is exposed to air during filtration (**Figure 2b**). The height distribution of the top surface measured by laser microscope is

14.5 ± 5.1 μm (**Figure 2c**), while that of the bottom surface is only 12.8 ± 2.2 μm (**Figure 2d**). It

is assumed that the smoothness of the bottom surface reflects the smoothness of the PTFE

membrane (**Figure S4**), while that of the top surface is largely affected by the degree of

agglomeration of the CNT/PBI/Pt dispersion. We decided that a comparison of MEAs with these

two different surfaces at the interface between the PEM and CL is useful for understanding the

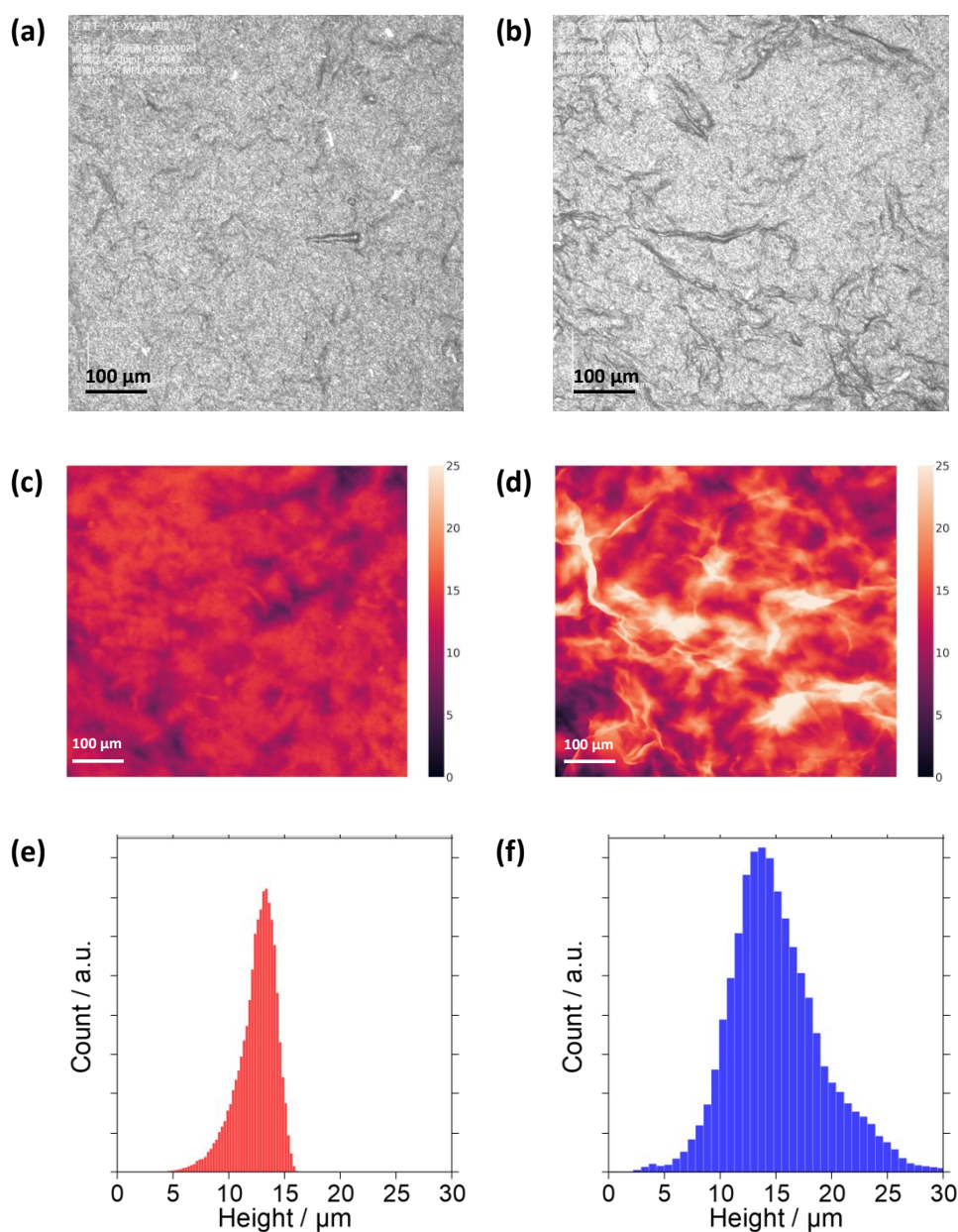effect of interfacial roughness on PEMFC performance.

Figure 2. (a, b) Optical microscope and (c, d) laser microscope images of (a, c) bottom surface and (b, d) top surface of CNT/PBI/Pt sheets. Scale bars: 100 μm. Height distribution histograms of (e) top and (f) bottom surfaces of the CNT/PBI/Pt sheets.

3.2 Fabrication and characterization of MEAs

Before the CNT/PBI/Pt sheets were used as the CLs, the ionomer was incorporated to CNT/PBI/Pt sheets because the obtained sheets did not contain ionomers. The ionomer was incorporated by dipping the sheets into Nafion solution (1.0 wt. %) for 24 h at 25 °C to ensure the adsorption equilibrium and the amount of the adsorption amount of the ionomer was controlled by the concentration of the ionomer solution. We have reported that PBI layer coated on the carbon surface facilitated Nafion adsorption and enabled homogeneous ionomer distribution in the CL [62], thus we consider that ionomer distribution in the MEAs is homogeneous throughout the CL. The ionomer content was evaluated using TGA according to a reported procedure [55], in which the sheets were heated from 30 to 550 °C under N_2 flow, followed by isothermal heating at 550 °C for 10 min to allow complete decomposition of the Nafion ionomer. Finally, the sample was heated from 200 to 900 °C under air flow to decompose the CNTs (**Figure S5a**). The weight reduction between 30 and 250 °C was caused by the evaporation of water from Nafion, and the decrease from 250 to 550 °C was due to the decomposition of Nafion (**Figure S5b**) [63]. Hence, the ratio of Nafion in the CL can be estimated by subtracting the weight reduction due to water evaporation from the composite weight after Nafion decomposition. The ionomer content in the CL was determined to be 27 wt%, corresponding to an ionomer/carbon (I/C) ratio of 0.43.
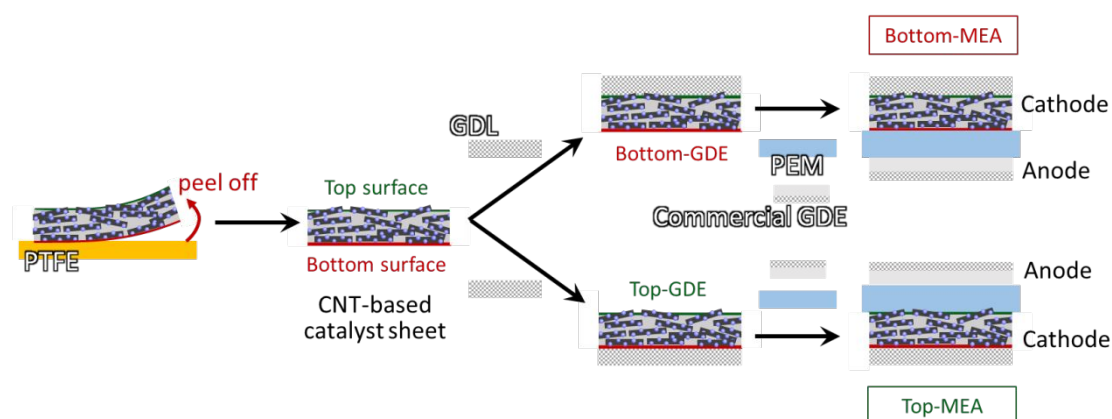
Scheme 2. Schematic of MEA fabrication: Vacuum filtration of CNT/PBI/Pt ink through PTFE filter membrane yields free-standing sheets, which are then laminated to GDLs, PEMs, and commercial GDEs to fabricate MEAs. MEAs having bottom-surface/PEM and top-surface/PEM interfaces are denoted as bottom-MEA and top-MEA, respectively.

To fabricate MEAs, a gas diffusion electrode (GDE) was laminated in such a way that exposes either the top surface (top-GDE) or bottom surface (bottom-GDE) of the CNT/PBI/Pt sheet when hot-pressed with a GDL. Then, the top-GDE or bottom-GDE was laminated on one side of the Nafion membrane, and a commercial GDE based on Pt/C was laminated on the other side by hot pressing to fabricate two separate MEAs, namely top-MEA and bottom-MEA, respectively (**Scheme 2**). Polarization curves for the top-MEA (**Figure 3a**) and bottom-MEA (**Figure 3a**) were measured at 80 °C under 100% relative humidity (RH) using H_2 and air at the anode and cathode, respectively. CNT-based CLs were used as cathode electrodes. We found that the bottom-MEA showed higher activity than the top-MEA in all current density regions, and the maximum power density of the bottom-MEA (604.6 mW cm^{-2}) was higher than that of the top-MEA (542.4 mW cm^{-2}) (**Figure S7**). Next, the ECSA of Pt in the MEAs was measured through in situ CV at 40 °C feeding H_2 and sustaining a N_2 atmosphere for the anode and cathode, respectively (**Figure 3b**; for separate graphs, refer to **Figure S6a** and **S6b**). Similar hydrogen adsorption/desorption peaks between 0.05 and 0.35 V (vs. RHE) were observed for both MEAs and the ECSA values were compared to estimate the difference of Pt environment between top-MEA and bottom-MEA. In

situ ECSA values for the top-MEA and bottom-MEA were 40.2 and 38.3 m^2 g^{-1}, respectively, indicating proton accessibility at the Pt interface is comparable for both CLs.
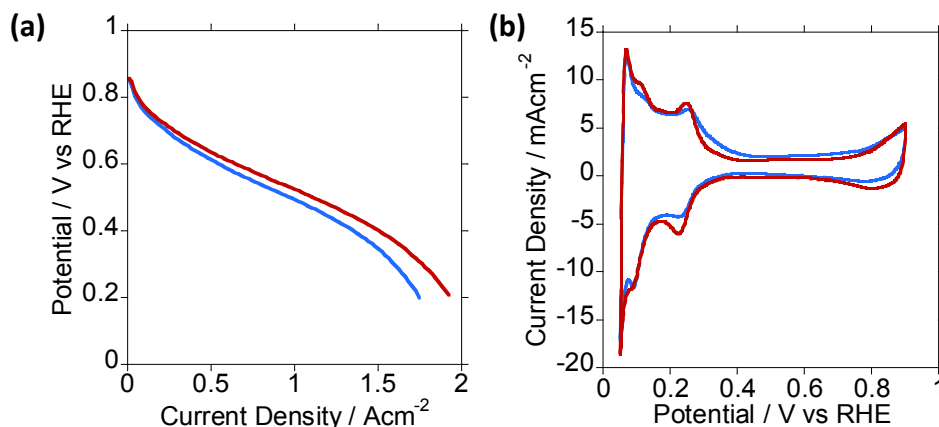

Figure 3. (a) I–V curves of top-MEA (blue) and bottom-MEA (red) measured at 80 °C and 100% RH, with H_2 and air fed to anode and cathode, respectively. (b) In situ CV curves of top-MEA (blue) and bottom-MEA (red) at 40 °C and 100% RH, with H_2 fed to anode and without gas flow for cathode.

To further study the performance of the two MEAs, electrochemical impedance spectroscopy (EIS) analysis of the MEAs was carried out (**Figure 4a** and **4b**) at current densities of 0.1 and 1.0 A cm^{-2}. These current densities were chosen because low (0.1 A cm^{-2}) and mid-current (1.0 A cm^{-2}) density regions are limited by charge transfer and ohmic resistance, respectively. The spectra were analyzed based on a typical equivalent circuit for PEMFCs (**Figure S1**) [64, 65], where the resistances are separated into ohmic resistance (R_Ω) that includes proton conduction resistance in the PEM as well as interface between the cathode CL and PEM (CL–PEM interface), charge transfer resistance (R_{ct}) mainly due to charge transfer resistance during the oxygen reduction reaction (ORR) at cathode Pt interface, and mass transport resistance (R_{mt}) related to the diffusion of O_2 in the CL and GDL. The values for each resistance are listed in **Table S1**. For bottom-MEA, R_Ω values remained almost unchanged ($\sim$ 0.14 Ω cm^2) (**Figure 4c**), while the R_{ct} and R_{mt} values decreased (**Figure 4d**) and increased (**Figure 4e**), respectively when the current density increased. Similar trends were also observed for top-MEA except for R_Ω that showed large decrease. The

trend for bottom-MEA is quite reasonable at 100% RH condition because the R_Ω was dominated by proton conductivity of the PEM, while R_{ct} and R_{mt} were dominated by charge transfer at Pt interface and oxygen diffusion in CL especially at low and high current density region, respectively [28]. Because the R_Ω values were higher than the estimated resistance of the PEM used (Nafion 212) (0.075 Ω cm^2 at 100% RH independent of the current density) [65], and all components were the same for the two MEAs except for the surface roughness of the cathode CL, we attribute the difference in R_Ω to the resistance at CL–PEM interface [66], where a larger R_Ω for the top-MEA indicates higher contact resistance of rough CL surface at the CL–PEM interface. We speculate the reason of the large decrease of R_Ω values for top-MEA as follows; the rough CL surface formed small air gap at PEM–CL interface even under 100% RH condition, resulting in large R_Ω. At high current density, the water generated filled the gap and supported the proton conduction, decreasing its R_Ω. Such water effect might cause high oxygen diffusion resistance as well at PEM–CL interface, leading to largely increased R_{mt} at 1.0 A cm^{-2} only for top-MEA (**Figure 4e**). Sung et al. reported that weak contact between PEM and CL increased not only R_Ω but also R_{ct} because of the slow ORR kinetic for cathode Pt at the CL–PEM interface[43]. In our case, larger R_{ct} for top-MEA at 0.1 A cm^{-2} might be due to the same reason. The higher performance for smoother CL over rough CL was also confirmed in different I/C (I/C = 0.29), where the bottom-MEA exhibited 10% higher maximum power density than top-MEA (**Figure S8**).
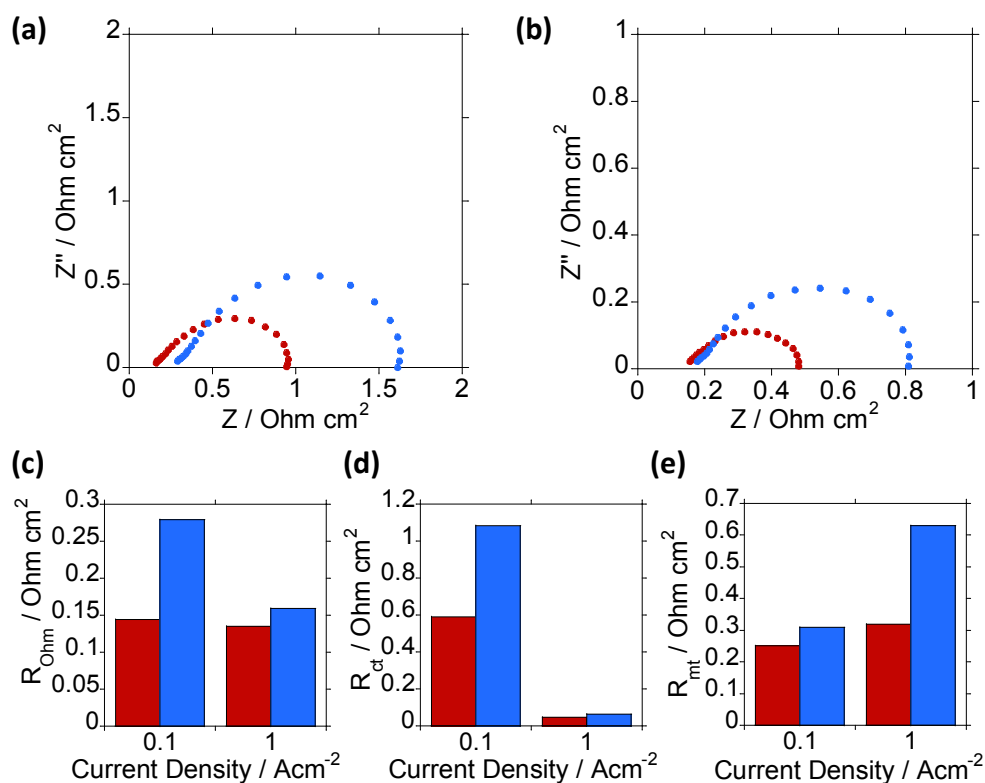
Figure 4. Impedance Nyquist plots of top-MEA (blue) and bottom-MEA (red) at 100% RH measured at (a) 0.1 A cm^{-2} and (b) 1.0 A cm^{-2}. Impedance of (c) R_Ω, (d) R_{ct}, and (e) R_{mt} for top-MEA (blue) and bottom-MEA (red) at 100% RH and 80 °C measured at 0.1 A cm^{-2} and 1 A cm^{-2}.

Through this study, we clearly demonstrate that the surface roughness of the CL affects the performance of PEMFCs containing CNT-based CLs, and a CNT-based CL with a smoother surface is preferable. To date, when CNT-based catalysts are embedded in the MEA, the CLs are often fabricated using the vacuum-filtration method, with a filter membrane as the filter medium instead of a GDL [29, 53, 54, 67]. However, differences in the CL surface roughness have not been reported thus far. It is shown in this study that providing contact between a CL, with a smoother surface, and the PEM is important, especially because CNTs agglomerate easily, forming CNT bundles on the top surface. In contrast to using a filter membrane as the filter medium, using a GDL results in the top surface being the only surface available to be used as the CL–PEM interface, which has a rougher surface. For such an MEA to perform better, the homogeneity of the surface must be well controlled such that the presence of CNT agglomerates is suppressed.

4. Conclusion

CNT-based GDEs were prepared using one-time sonication throughout the entire process. This innovative and facile process preserves the original properties, length, and other advantageous features of CNTs, opening up possibilities for the realization of extra-durable, high-performance PEMFCs when compared to current PEMFCs. Laser microscopy and optical microscopy observations showed that fabricating CNT-based CLs by vacuum filtration of the electrocatalyst dispersion through a filter membrane yielded a free-standing CNT electrocatalyst sheet with a different surface roughness on each of its two available surfaces. The polarization curve showed that for the cathode CL, placing the smoother CL surface in contact with the PEM resulted in a higher PEMFC performance (604.6 mW cm^{-2}) than that using the rougher CL surface (542.4 mW cm^{-2}). According to the EIS analysis, the higher performance obtained from laminating the smoother surface of the CL with the PEM is due to the lower interfacial resistance between the cathode CL and PEM, improving proton transport at the cathode CL and PEM interface. In summary, optimizing the surface of a CL-contacting PEM offers two advantages. First, it allows the fabrication of a high-performance CL using the versatile, simple, and fast vacuum-filtration method, lowering the fabrication cost of the CL, which is a vital PEMFC component. Second, it provides a one-step, simple improvement process for increasing the PEMFC performance when fabricating CLs by the vacuum-filtration method. Through continued optimization of the fabrication method used in this study, additional improvements in the PEMFC power density output can be expected. Although improving the Pt utilization efficiency of PEMFCs depends on numerous factors, we believe that the CL surface roughness for CNT-CLs is a significant consideration in enhancing this efficiency.

CRediT authorship contribution statement

16

Yin Kan Phua: Investigation and Writing - Original Draft. **Don Terrence Dhammika Weerathunga**: Investigation. **Dan Wu**: Investigation. **Chaerin Kim**: Investigation. **Naoki Tanaka**: Investigation. **Samindi Madhubha Jayawickrama**: Investigation. **Tsuyohiko Fujigaya**: Conceptualization, Supervision, Writing-Review & Editing.

Conflicts of Interest

The authors declare that they have no known competing financial interests or personal relationships that could have influenced the work reported in this study.

References

1. T. Klaiber, *J. Power Sources*, 1996, **61**, 61-69.
2. W. Dönitz, *Int. J. Hydrogen Energy*, 1998, **23**, 611-615.
3. K. Jiao, J. Xuan, Q. Du, Z. Bao, B. Xie, B. Wang, Y. Zhao, L. Fan, H. Wang, Z. Hou, S. Huo, N. P. Brandon, Y. Yin and M. D. Guiver, *Nature*, 2021, **595**, 361-369.
4. N. P. Brandon, S. Skinner and B. C. H. Steele, *Annual Review of Materials Research*, 2003, **33**, 183-213.
5. A. Esmaeilifar, S. Rowshanzamir, M. H. Eikani and E. Ghazanfari, *Energy*, 2010, **35**, 3941-3957.
6. Y. Wang, D. F. Ruiz Diaz, K. S. Chen, Z. Wang and X. C. Adroher, *Mater. Today*, 2020, **32**, 178-203.
7. G. S. Avcioglu, B. Ficicilar and I. Eroglu, *Int. J. Hydrogen Energy*, 2018, **43**, 10779-10797.
8. X. X. Wang, M. T. Swihart and G. Wu, *Nature Catalysis*, 2019, **2**, 578-589.

9. Y.-J. Wang, B. Fang, H. Li, X. T. Bi and H. Wang, *Prog. Mater Sci.*, 2016, **82**, 445-498.
10. E. H. Majlan, D. Rohendi, W. R. W. Daud, T. Husaini and M. A. Haque, *Renewable Sustainable Energy Rev.*, 2018, **89**, 117-134.
11. S. Zhang, Y. Shao, G. Yin and Y. Lin, *J. Mater. Chem. A*, 2013, **1**.
12. R. E. Yonoff, G. V. Ochoa, Y. Cardenas-Escorcia, J. I. Silva-Ortega and L. Merino-Stand, *Heliyon*, 2019, **5**, e01724.
13. K. H. Kangasniemi, D. A. Condit and T. D. Jarvi, *J. Electrochem. Soc.*, 2004, **151**, E125-E132.
14. K. Kinoshita and J. A. S. Bett, *Carbon*, 1973, **11**, 403-411.
15. T. Fujigaya, S. Hirata, M. R. Berber and N. Nakashima, *ACS Appl. Mater. Interfaces*, 2016, **8**, 14494-14502.
16. X. Wang, W. Li, Z. Chen, M. Waje and Y. Yan, *J. Power Sources*, 2006, **158**, 154-159.
17. D. A. Stevens and J. R. Dahn, *Carbon*, 2005, **43**, 179-188.
18. S. Jayabal, G. Saranya, D. Geng, L.-Y. Lin and X. Meng, *J. Mater. Chem. A*, 2020, **8**, 9420-9446.
19. L. Li and Y. Xing, *J. Electrochem. Soc.*, 2006, **153**, A1823-A1828.
20. H. Dai, *Acc. Chem. Res.*, 2002, **35**, 1035-1044.
21. E. Dujardin, T. W. Ebbesen, H. Hiura and K. Tanigaki, *Science*, 1994, **265**, 1850-1852.
22. Z. Liu, X. Lin, J. Y. Lee, W. Zhang, M. Han and L. M. Gan, *Langmuir*, 2002, **18**, 4054-4060.
23. M. Tominaga, Y. Yatsugi and M. Togami, *RSC Adv.*, 2014, **4**, 53833-53836.
24. L. Ye, Y. Gao, J. Zheng and P. Li, *ECS Transactions*, 2015, **66**, 1-9.
25. X. Wang, M. Waje and Y. Yan, *Electrochem. Solid-State Lett.*, 2005, **8**, A42-A44.
26. Z. Yang, T. Fujigaya and N. Nakashima, *J. Power Sources*, 2015, **300**, 175-181.
27. C. Paoletti, A. Cemmi, L. Giorgi, R. Giorgi, L. Pilloni, E. Serra and M. Pasquali, *J. Power Sources*, 2008, **183**, 84-91.
28. J.-J. Sun, H.-Z. Zhao, Q.-Z. Yang, J. Song and A. Xue, *Electrochim. Acta*, 2010, **55**, 3041-3047.
29. S. Zhu, J. Zheng, J. Huang, N. Dai, P. Li and J. P. Zheng, *J. Power Sources*, 2018, **393**, 19-31.
30. Q. Zhang, Y. Ling, W. Cai, X. Yu and Z. Yang, *Int. J. Hydrogen Energy*, 2017, **42**, 16714-16721.
31. M. Okamoto, T. Fujigaya and N. Nakashima, *Adv. Funct. Mater.*, 2008, **18**, 1776-1782.
32. T. Fujigaya, M. Okamoto and N. Nakashima, *Carbon*, 2009, **47**, 3227-3232.
33. M. Okamoto, T. Fujigaya and N. Nakashima, *Small*, 2009, **5**, 735-740.
34. K. Matsumoto, T. Fujigaya, K. Sasaki and N. Nakashima, *J. Mater. Chem.*, 2011, **21**, 1187-1190.
35. M. R. Berber, I. H. Hafez, T. Fujigaya and N. Nakashima, *Sci. Rep.*, 2015, **5**, art. no. 16711.
36. T. A. M. Suter, K. Smith, J. Hack, L. Rasha, Z. Rana, G. M. A. Angel, P. R. Shearing, T. S. Miller and D. J. L. Brett, *Adv. Energy Mater.*, 2021, **11**.
37. T. Suzuki, R. Hashizume and M. Hayase, *J. Power Sources*, 2015, **286**, 109-117.
38. D. T. D. Weerathunga, S. M. Jayawickrama, Y. K. Phua, K. Nobori and T. Fujigaya, *Bull. Chem. Soc. Jpn.*, 2019, **92**, 2038-2042.
39. H. Li, Y. Tang, Z. Wang, Z. Shi, S. Wu, D. Song, J. Zhang, K. Fatih, J. Zhang, H. Wang, Z. Liu, R. Abouatallah and A. Mazza, *J. Power Sources*, 2008, **178**, 103-117.
40. A. H. Kakaee, G. R. Molaeimanesh and M. H. Elyasi Garmaroudi, *Int. J. Hydrogen Energy*, 2018, **43**, 15481-15491.
41. H. Tang, S. Wang, S. P. Jiang and M. Pan, *J. Power Sources*, 2007, **170**, 140-144.
42. C.-Y. Liu and C.-C. Sung, *J. Power Sources*, 2012, **220**, 348-353.

43. C.-C. Sung, C.-Y. Liu and C. C. J. Cheng, *Int. J. Hydrogen Energy*, 2014, **39**, 11700-11705.
44. S. Shahgaldi, I. Alaefour and X. Li, *Appl. Energy*, 2018, **225**, 1022-1032.
45. J. Yu, N. Grossiord, C. E. Koning and J. Loos, *Carbon*, 2007, **45**, 618-623.
46. T. Suzuki, S. Tsushima and S. Hirai, *Int. J. Hydrogen Energy*, 2011, **36**, 12361-12369.
47. I.-S. Park, W. Li and A. Manthiram, *J. Power Sources*, 2010, **195**, 7078-7082.
48. M. S. Wilson and S. Gottesfeld, *J. Appl. Electrochem.*, 1992, **22**, 1-7.
49. J. Xie, F. Garzon, T. Zawodzinski and W. Smith, *J. Electrochem. Soc.*, 2004, **151**.
50. G. Bender, T. A. Zawodzinski and A. P. Saab, *J. Power Sources*, 2003, **124**, 114-117.
51. S. Moller-Holst, *Denki Kagaku oyobi Kogyo Butsuri Kagaku*, 1996, **64**, 699-705.
52. B. Millington, V. Whipple and B. G. Pollet, *J. Power Sources*, 2011, **196**, 8500-8508.
53. W. Z. Li, X. Wang, Z. W. Chen, M. Waje and Y. S. Yan, *Langmuir*, 2005, **21**, 9386-9389.
54. W. Z. Li, X. Wang, Z. W. Chen, M. Waje and Y. S. Yan, *J. Phys. Chem. B*, 2006, **110**, 15353-15358.
55. M. Kishi, M. Tanaka and T. Mori, *Journal of the Society of Powder Technology, Japan*, 2020, **57**, 4-11.
56. N. E. a. I. T. D. Organization, *NEDO Cell Evaluation and Analysis Protocol*, New Energy and Industrial Technology Development Organization, 2012.
57. T. Fujigaya and N. Nakashima, *Adv. Mater.*, 2013, **25**, 1666-1681.
58. P. Vichchulada, M. A. Cauble, E. A. Abdi, E. I. Obi, Q. Zhang and M. D. Lay, *J. Phys. Chem. C*, 2010, **114**, 12490-12495.
59. W. Huang, Y. Lin, S. Taylor, J. Gaillard, A. M. Rao and Y.-P. Sun, *Nano Lett.*, 2002, **2**, 231-234.
60. M. D. Rossell, C. Kuebel, G. Ilari, F. Rechberger, F. J. Heiligtag, M. Niederberger, D. Koziej and R. Erni, *Carbon*, 2013, **61**, 404-411.
61. K. L. Lu, R. M. lago, Y. K. Chen, M. L. H. Green, P. J. F. Harris and S. C. Tsang, *Carbon*, 1996, **34**, 814-816.
62. S. M. Jayawickrama, D. Wu, R. Nakayama, S. Ishikawa, X. Liu, G. Inoue and T. Fujigaya, *J. Power Sources*, 2021, **496**, 229855.
63. S. R. Samms, S. Wasmus and R. F. Savinell, *J. Electrochem. Soc.*, 1996, **143**, 1498-1504.
64. S. Cruz-Manzo and R. Chen, *J. Electroanal. Chem.*, 2013, **694**, 45-55.
65. J. Santana, M. Espinoza-Andaluz, T. Li and M. Andersson, *Frontiers in Energy Research*, 2020, **8**.
66. S. Asghari, A. Mokmeli and M. Samavati, *Int. J. Hydrogen Energy*, 2010, **35**, 9283-9290.
67. F. Luo, Y. Ling, Q. Zhang, X. Yu, Q. Liu and Z. Yang, *J. Mater. Sci.*, 2017, **52**, 8412-8420.